Supporting Information

Multi-site catalysis of high-entropy hydroxides for sustainable electrooxidation of glucose to glucaric acid

Xianhong Wu, ‡[a,g] Zhi-Jian Zhao,‡[b] Xiangcheng Shi,‡[b,h] Liqun Kang,[c] Pratteek Das,[a] Sen Wang,[a] Shengqi Chu,[d] Hua Wang,[e] Kenneth Davey,[f] Bo Zhang,*[e] Shi-Zhang Qiao, *[f] Jinlong Gong*[b] and Zhong-Shuai Wu*[a,i]

Materials and Methods

Synthesis of D-FeCoNiCu-LDH/NF electrocatalyst

First, FeCoNiCuCr-LDH/NF was synthesized *via* electrodeposition. Ni foam, graphite rod and an Ag/AgCl electrode saturated with KCl solution were used as the, respectively, working, counter and reference, electrode. Potentiostatic deposition of FeCoNiCuCr-LDH-LDH was carried out at −1.0 V for 600 s at room temperature on a CHI 760E electrochemical workstation. The electrolyte was a mix of 0.12 M $Ni(NO_3)_2 \cdot 6H_2O$, $Co(NO_3)_2 \cdot 6H_2O$, $Cu(NO_3)_2 \cdot 3H_2O$, $Cr(NO_3)_3 \cdot 9H_2O$ and $Fe(NO_3)_3 \cdot 9H_2O$ aqueous solutions with a molar ratio of 1:1:1:1:1. For comparison, FeCoNiCu-LDH/NF, FeNiCuCr-LDH/NF, FeCoCuCr-LDH/NF and FeCoNiCr-LDH/NF were synthesized under similar conditions in the absence of $Cr(NO_3)_3 \cdot 9H_2O$, $Co(NO_3)_2 \cdot 6H_2O$, $Ni(NO_3)_2 \cdot 6H_2O$ or $Cu(NO_3)_2 \cdot 3H_2O$, respectively, of corresponding electrolyte. D-FeCoNiCu-LDH/NF is synthesized *via* electrochemical activation of consecutive CV cyclic scan of 500 sweeps between 1.0 to 1.5 V *vs.* RHE in 1.0 M KOH at a scan of 50 mV s^{-1} with FeCoNiCu-LDH/NF as working electrode, graphite rod as counter, and Hg/HgO electrode saturated with 1.0 M KOH solution as reference electrode.

Material Characterization

Morphology was characterized *via* SEM (Quanta 200F), TEM (HT7700), HRTEM (JEM-F200) and spherical aberration-corrected TEM (ARM300). Microstructure and phase of samples was determined *via* XRD (SmartLab, Cu Kα radiation). The surface /internal characteristics for samples were established using Thermo ESCALAB MK II XPS. The mass ratio for Fe, Co, Ni, Cu and Cr elements was established *via* ICP-OES (PerkinElmer Optima 7300DV). The *operando* Raman spectra was recorded on LabRAM HR 800 using a 532 nm laser during OER and GOR. XANES and EXAFS data were collected in the BL14W1 and 1W1B beamline, of the Shanghai and Beijing Synchrotron Radiation Facility (SSRF and BSRF).

Data processing for XAFS spectra

XAFS spectra were analyzed using the Demeter software package (version 0.9.26, including Athena and Artemis program package).[1] Pre-edge background subtraction, post-edge normalization and forward Fourier Transform of XAS data were processed using the Athena program. A linear regression background (-150 to -30 eV refers to E_0

position) was determined, and a quadratic polynomial regression for post-edge normalization was applied (+100 to +590 eV refers to E_0 position). The spectra were splined from $k = 0$ to $k = 12$ Å^{-1} (548 eV after the edge) with Rbkg of 1.0 and k-weight of 2. The k^2-weighted R-space EXAFS spectra were fitted within R range of 1-3 Å and k range of 2.5-10.5 Å^{-1}. The amplitude reduction factors S_0^2 were determined to be 0.72, 0.72, 0.79 and 0.95 by fitting of k^2-weighted R-space EXAFS of Fe, Co, Ni and Cu -foil based on standard crystal parameters for, respectively, Fe, Co, Ni and Cu metal, and was used as fixed parameter for EXAFS fitting for FeCoNiCuCr-LDH and D-FeCoNiCu-LDH.

Half-cell GOR test

Electrocatalytic performance of electrocatalysts was established on a CHI 760E electrochemical workstation with a standard three-electrode system. The *as-prepared* samples were directly used as working electrode, a graphite rod was used as counter, and an Hg/HgO electrode saturated with 1M KOH solution was used as reference electrode. The electrolyte was 1.0 M KOH containing glucose (0 to 120 mM). LSV was measured with *iR* compensation. Tafel slopes were determined *via* fitting the linear regions to the Tafel equation, $\eta = b \log |j| + a$, *via* re-plotting of the polarization curves. EIS measurements were determined at selected overpotentials in the frequency range 100 kHz to 1 Hz and an amplitude of 5 mV at 1.2 V *vs.* RHE.

Assembly and tests of the two-electrode electrolyzer

Electrochemical hybrid electrolyzer was used with D-FeCoNiCu-LDH/NF as anode and FeCoNiCuCr-LDH/NF as cathode, with a cation exchange membrane separating the anodic- (1.0 M KOH with 0.1 M glucose) and cathodic- (1.0 M KOH with 0.1 M KNO_3) -chambers Electrolysis tests were performed on a CHI 760E electrochemical workstation. Polarization curves were measured with *iR* compensation. The stability test was determined at controlled current density without *iR* compensation.

***In Situ* Raman spectra**

In situ Raman analysis was determined on LabRAM HR 800 with an excitation wavelength of 532 nm. *In situ* spectro-electrochemical experiments were established in a custom-designed electrochemical cell with Ag/AgCl as reference and, Pt wire as counter, electrode and, the prepared catalyst as working electrode. Raman signals were recorded *in situ* as open-circuit voltage and applied potential.

Product Analyses

Concentration changes in glucose and oxidation products in electrolysis were monitored *via* high performance liquid chromatography (HPLC) equipped with a refractive index detector. In each analysis, 0.9 mL of the electrolyte solution was withdrawn from the electrochemical cell in the chronoamperometry test, and diluted with 1.0 M phosphate (H_3PO_3, 0.4 mL) solution to adjust pH < 7.0.

Glucose concentration. Sulfuric acid (H_2SO_4) 5 mM was used as the mobile phase with a constant flow of 0.5 mL min^{-1}. 10 μL of the diluted electrolyte solution was injected directly into a BioRad Aminex 87H column, with a column temperature of 35 ^oC.

Glucaric and gluconic acid concentration. Dipotassium hydrogen phosphate and tetrabutylammonium hydrogen sulfate solution was used as the mobile phase with a constant flow of 0.7 mL min^{-1}. 10 μL of the diluted electrolyte solution was injected directly into a Kromasil C_{18} column, with a column temperature of 35 ^oC.

Theoretical Computation

Global structural search. The most stable surface of FeCoNiCu-LDH was determined *via* an evolutionary algorithm (EA)-based-structure-search; a global search of natural selection where the 'fittest' individuals are selected for reproduction to produce offspring for the next generation. The improved efficiency of EA for HEMs complex chemical space has been reported.[2, 3] An initial set of structures is initially generated at random within appropriate limits for the cell shape and interatomic distances,[4] that is relaxed and evaluated with density functional theory (DFT). The initial set of structures is used to 'train' a Gaussian process regression (GPR) model. GPR was trained separately for each tribe to obviate highly significant computations and 'large' datasets.[5] The number of DFT computations was significantly reduced. A co-evolution framework was adopted to simulate (actual) evolution in which individual populations develop in isolation and periodically interact with neighboring tribes.

The template structure for structure-search was a (4×4) NiOOH one-layer model. The arrangement for Fe, Co, Ni, Cu and the location of H atoms (to maintain structural stability of NiOOH one-layer model) was used as an adjustment during the structure-search. A configuration of alloy arrangement and location of H atoms can be seen analogously as a chromosome. The free energy computed from DFT following fully, local relaxation was used as a fitness function in EA to determine a structure that was

the most thermodynamically favorable. Importantly, the structure determined has the possibility to be the most abundant phase in the reaction.[6] The structure-search was initiated with 20 randomly generated structures with different chromosomes. Successive generations were simulated with a series of structural operators to generate new structures from current ones, including recombination and mutation. Those structures with low free energy are more likely to be selected for generating new structures, whilst those with high energy are rejected. 100 generations were used to identify the stable surface of D-FeCoNiCu-LDH/NF, and each generation maintained a population size of 5. Convergence was determined because the energy searching curves do not decrease for tens of generations.

DFT. DFT computations were determined with the plane-wave-based Vienna *Ab initio* Simulation package, VASP.[7] Electron exchange and correlation were described by the generalized gradient approximation (GGA) in the form of the Perdew-Burke-Ernzerhof (PBE) functional.[8] Electron-ion interactions were described within the projector-augmented wave framework.[9] In all computations the energy cutoff of the plane-wave basis was 400 eV. Optimized structures were established *via* minimizing forces on each ion until they were < 0.02 eV/Å. A reciprocal space-mesh of gamma points was used for Brillouin zone integration.

High-throughput screening of adsorption sites. To establish the multiple active sites of D-FeCoNiCu-LDH/NF for GOR, a high-throughput screening amongst possible adsorption configurations of the intermediates was determined. For each intermediate, the adsorption energy of multiple possible adsorption sites was generated and, initially, the adsorbent was placed as highlighted in Fig. S20. During local relaxation, the adsorption configuration can change dynamically, and the adsorbent of the relaxed structure does not need to remain in its initial site. Findings for the high-throughput screening are presented as Tables S4 to S10, and Figs. S20 to S22.

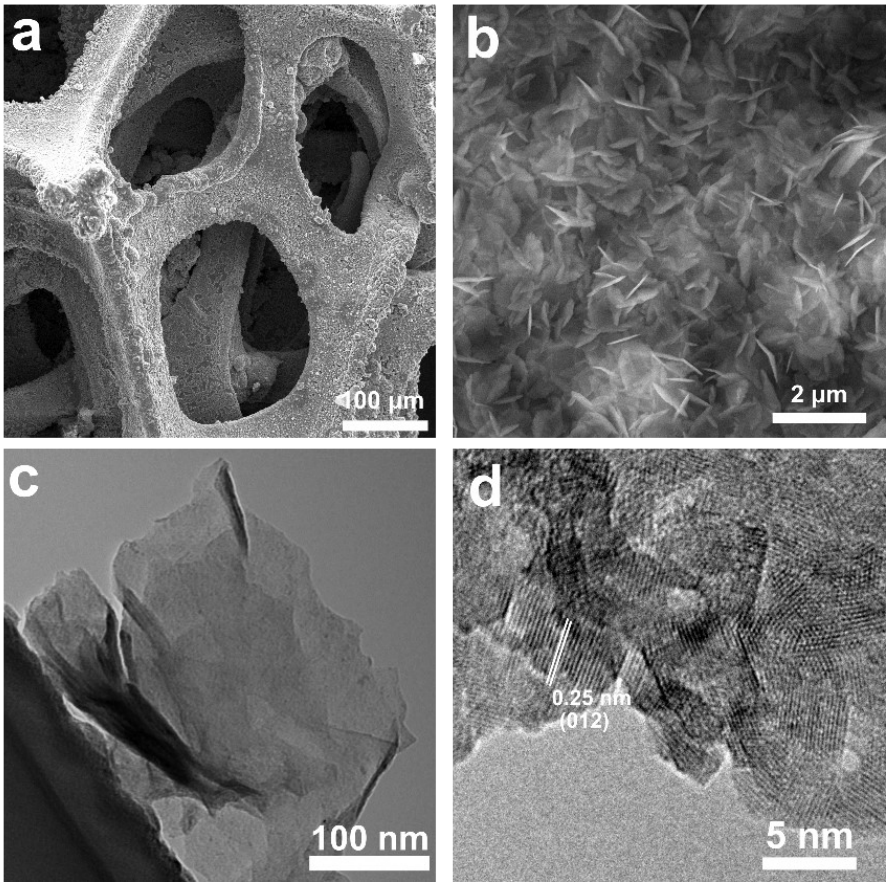

Figure S1. (a-b) SEM images of FeCoNiCuCr-LDH/NF. (c) TEM and (d) HRTEM images of FeCoNiCuCr-LDH peeled from NF.

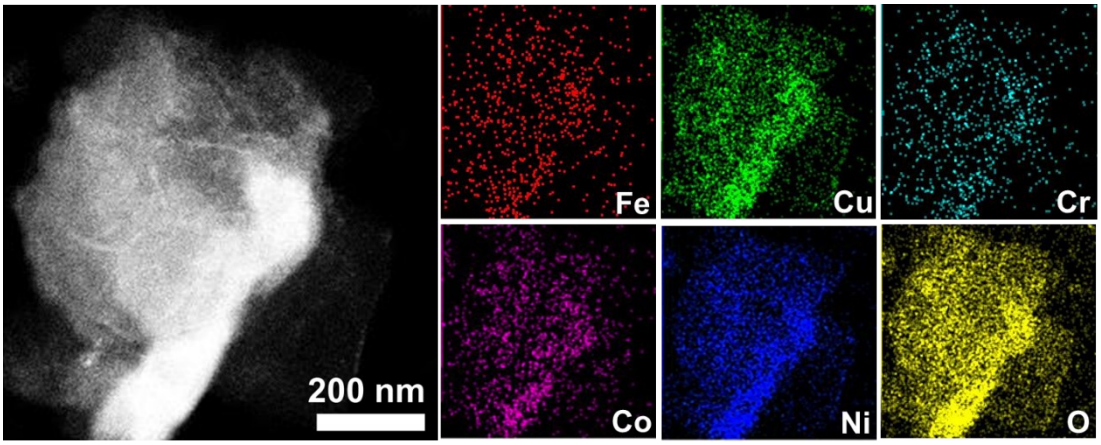

Figure S2. Elemental mapping evidencing the presence and homogenous distribution of Fe, Co, Ni, Cu, Cr and O elements in FeCoNiCuCr-LDH.

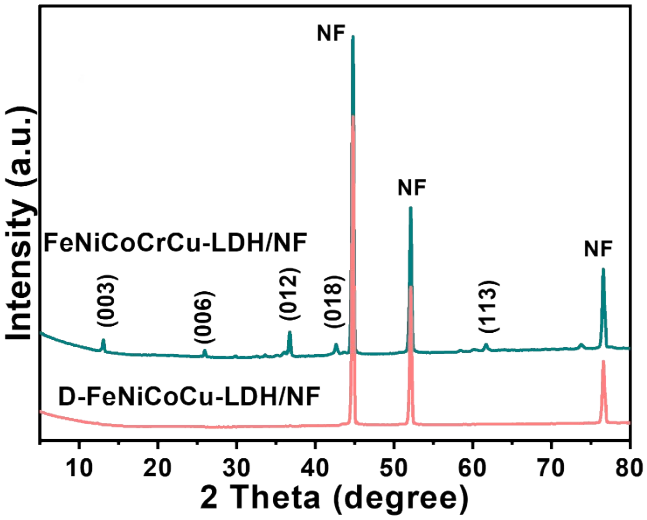

Figure S3. XRD patterns for FeCoNiCuCr-LDH/NF and D-FeNiCoCu-LDH/NF.

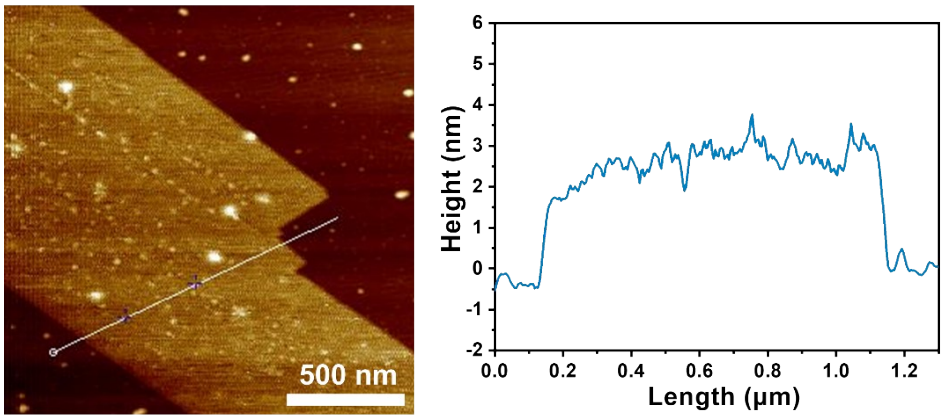

Figure S4. AFM image of D-FeCoNiCu-LDH with uniform thickness of *ca*. 2 to 3 nm.

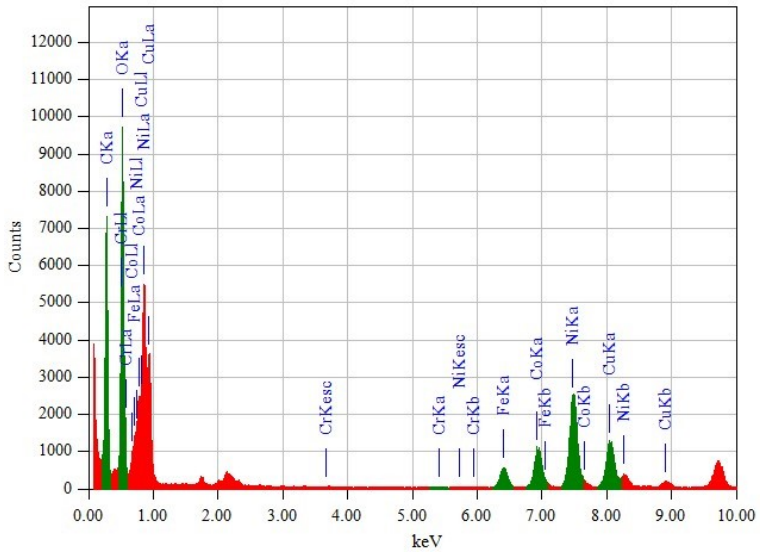

Figure S5. EDS spectra for D-FeCoNiCu-LDH.

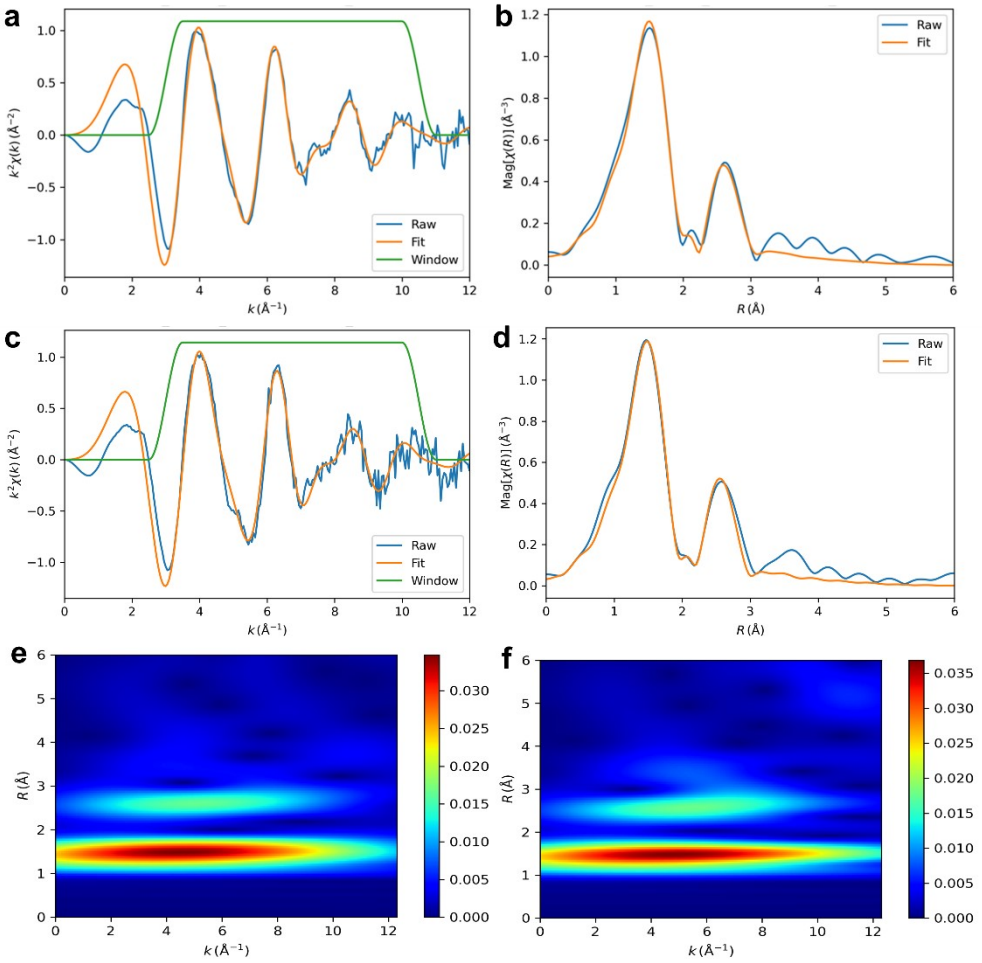

Figure S6. Fitted results for Fe K-edge EXAFS. (a) k^2-weighted k-space EXAFS for FeCoNiCuCr-LDH. (b) k^2-weighted R-space FT-EXAFS for FeCoNiCuCr-LDH. (c) k^2-weighted k-space EXAFS for D-FeCoNiCu-LDH. (d) k^2-weighted R-space FT-EXAFS for D-FeCoNiCu-LDH. (e) k^2-weighted Wavelet-Transform EXAFS (WT-EXAFS) for FeCoNiCuCr-LDH. (f) k^2-weighted WT-EXAFS for D-FeCoNiCu-LDH. (Fitted parameters are presented in Table S1).

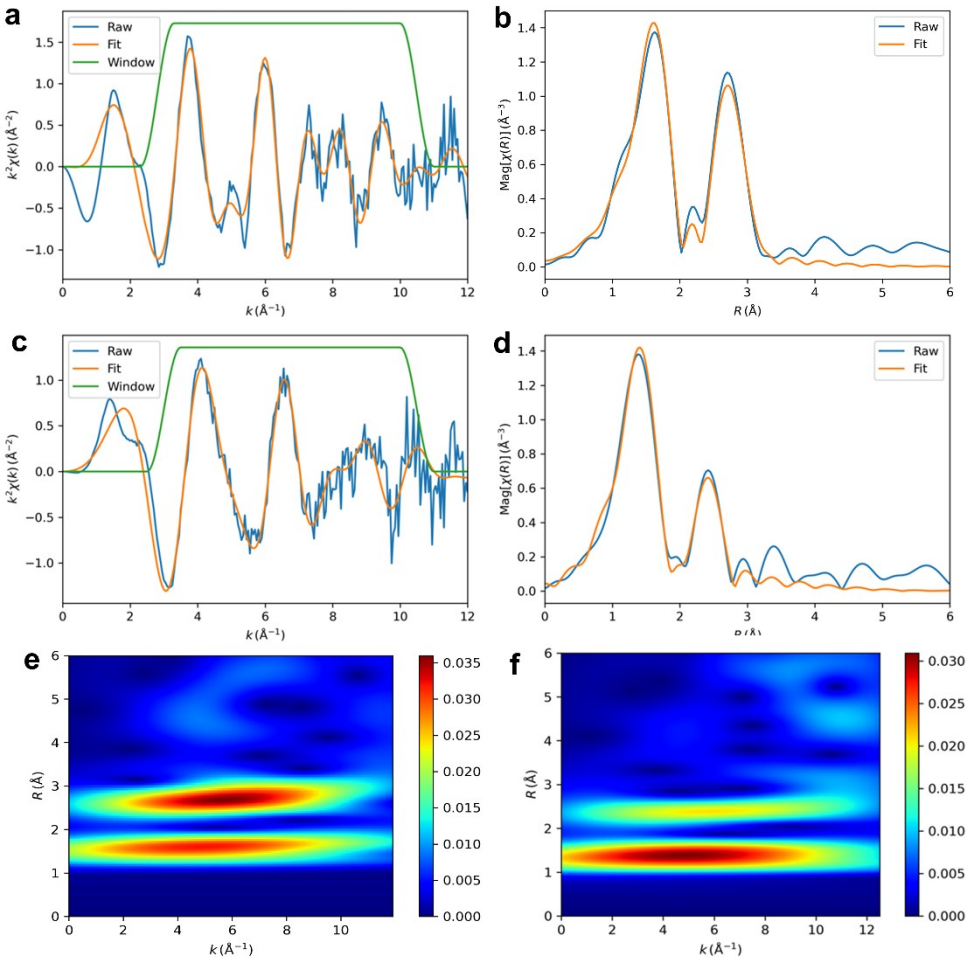

Figure S7. Fitted results for Co K-edge EXAFS. (a) k^2-weighted k-space EXAFS for FeCoNiCuCr-LDH. (b) k^2-weighted R-space FT-EXAFS for FeCoNiCuCr-LDH. (c) k^2-weighted k-space EXAFS for D-FeCoNiCu-LDH. (d) k^2-weighted R-space FT-EXAFS for D-FeCoNiCu-LDH. (e) k^2-weighted Wavelet-Transform EXAFS (WT-EXAFS) for FeCoNiCuCr-LDH. (f) k^2-weighted WT-EXAFS for D-FeCoNiCu-LDH. (Fitted parameters are presented in Table S1).

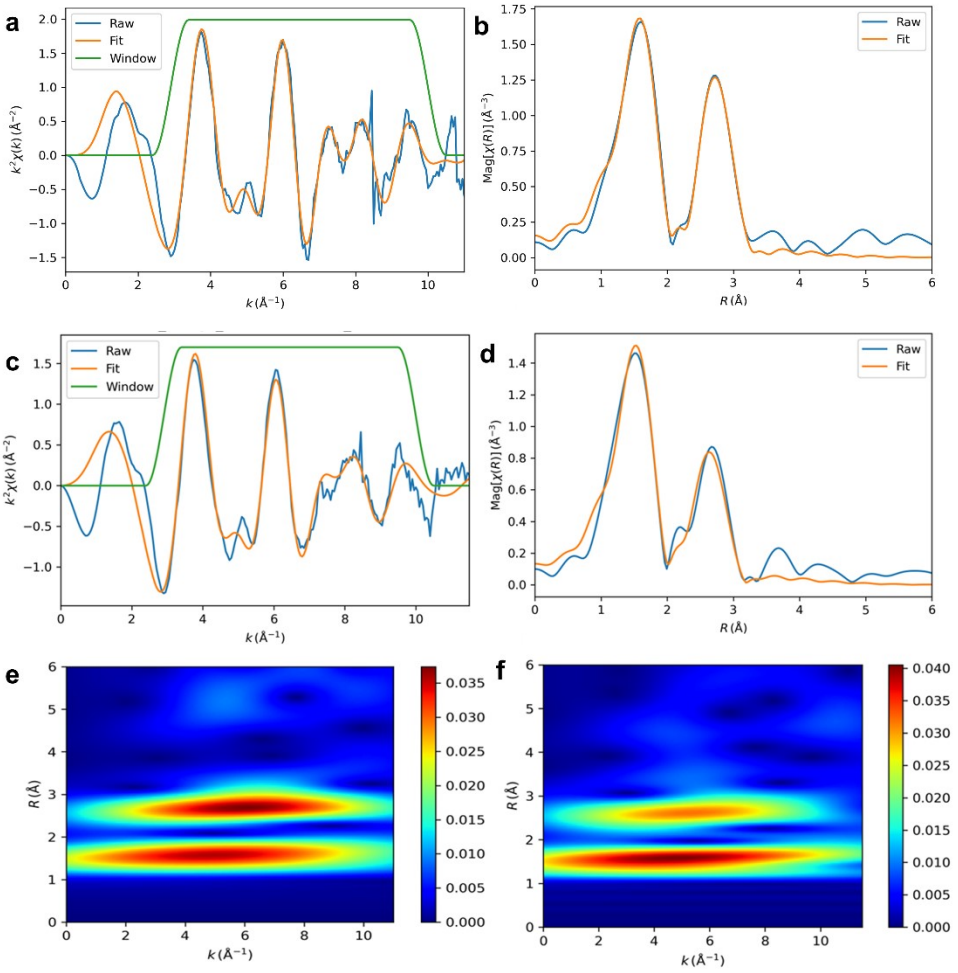

Figure S8. Fitted results for Ni K-edge EXAFS. (a) k^2-weighted k-space EXAFS for FeCoNiCuCr-LDH. (b) k^2-weighted R-space FT-EXAFS for FeCoNiCuCr-LDH. (c) k^2-weighted k-space EXAFS for D-FeCoNiCu-LDH. (d) k^2-weighted R-space FT-EXAFS for D-FeCoNiCu-LDH. (e) k^2-weighted Wavelet-Transform EXAFS (WT-EXAFS) for FeCoNiCuCr-LDH. (f) k^2-weighted WT-EXAFS for D-FeCoNiCu-LDH. (Fitted parameters are presented in Table S1).

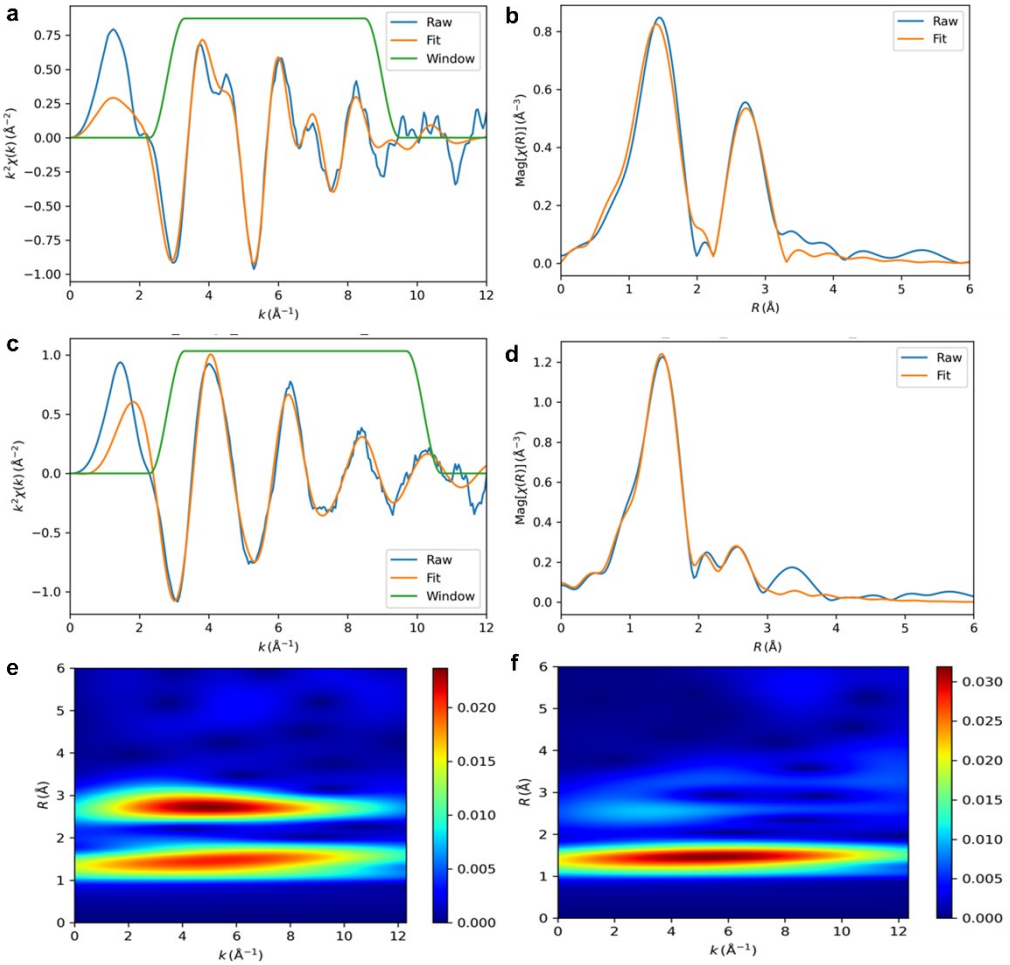

Figure S9. Fitted results for Cu K-edge EXAFS. (a) k^2-weighted k-space EXAFS for FeCoNiCuCr-LDH. (b) k^2-weighted R-space FT-EXAFS for FeCoNiCuCr-LDH. (c) k^2-weighted k-space EXAFS for D-FeCoNiCu-LDH. (d) k^2-weighted R-space FT-EXAFS for D-FeCoNiCu-LDH. (e) k^2-weighted Wavelet-Transform EXAFS (WT-EXAFS) for FeCoNiCuCr-LDH. (f) k^2-weighted WT-EXAFS for D-FeCoNiCu-LDH. (Fitted parameters are presented in Table S1).

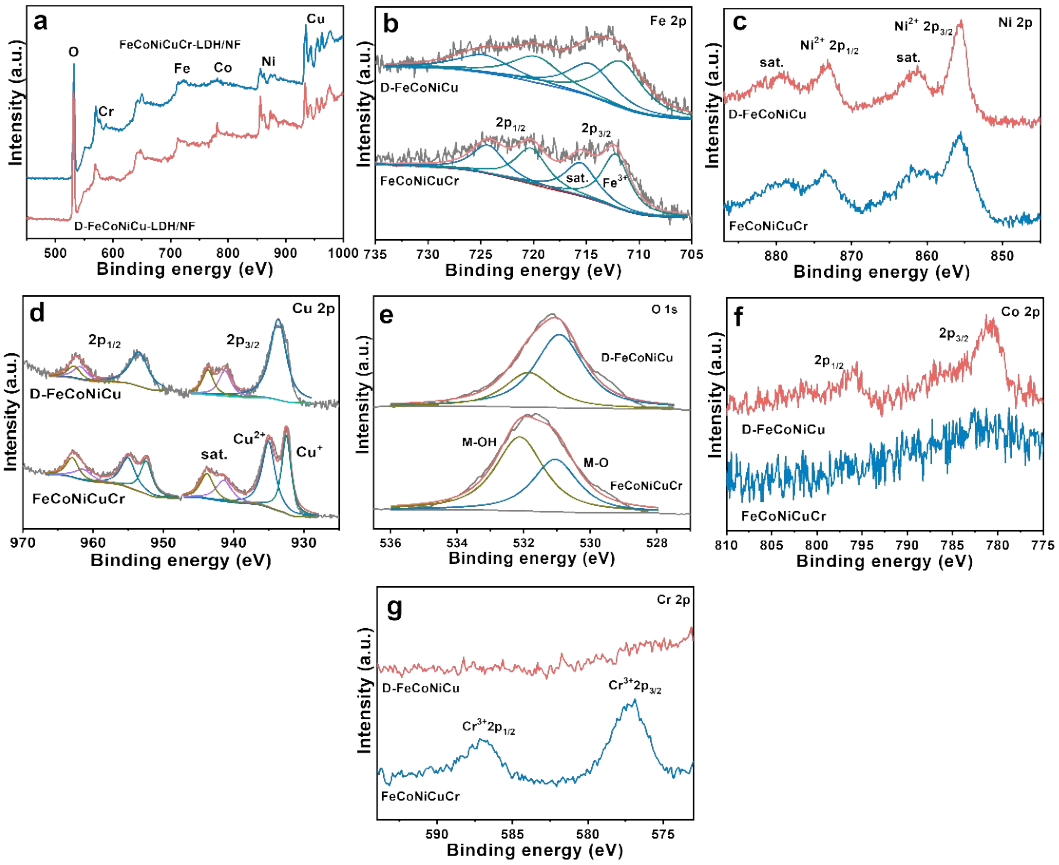

Figure S10. (a) XPS survey scan, (b) Fe 2p, (c) Cu 2p, (d) Ni 2p, (e) O1s, (f) Co 2p and (g) Cr 2p XPS spectra for FeCoNiCuCr-LDH/NF and D-FeCoNiCu-LDH/NF.

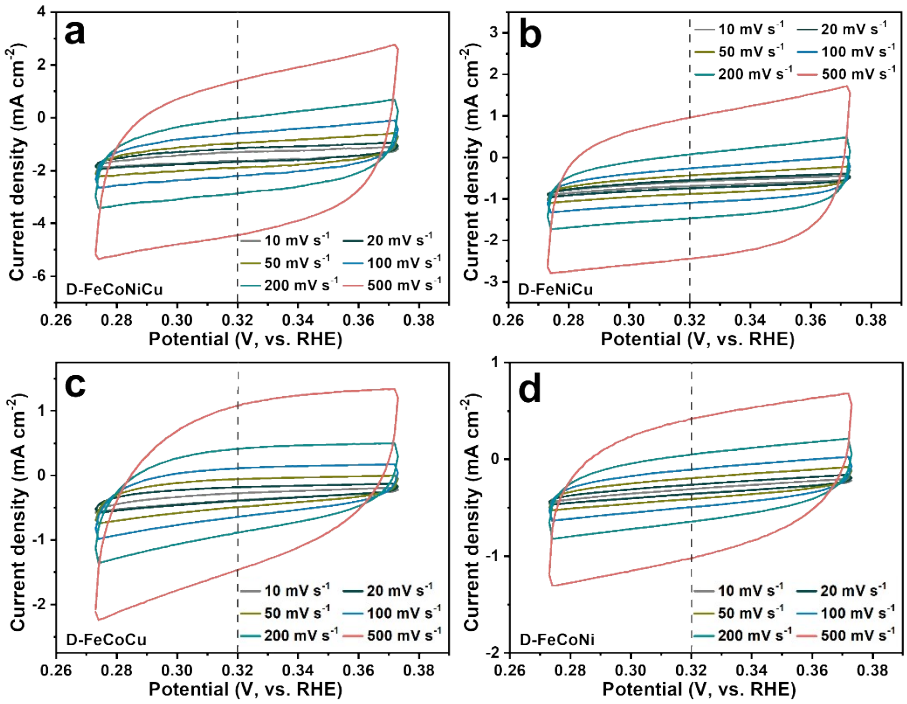

Figure S11. The CVs of (a) D-FeCoNiCu-LDH/NF, (b) D-FeNiCu-LDH/NF, (c) D-FeCoCu-LDH/NF and (d) D-FeCoNi-LDH/NF in 1.0 M KOH with 100 mM glucose.

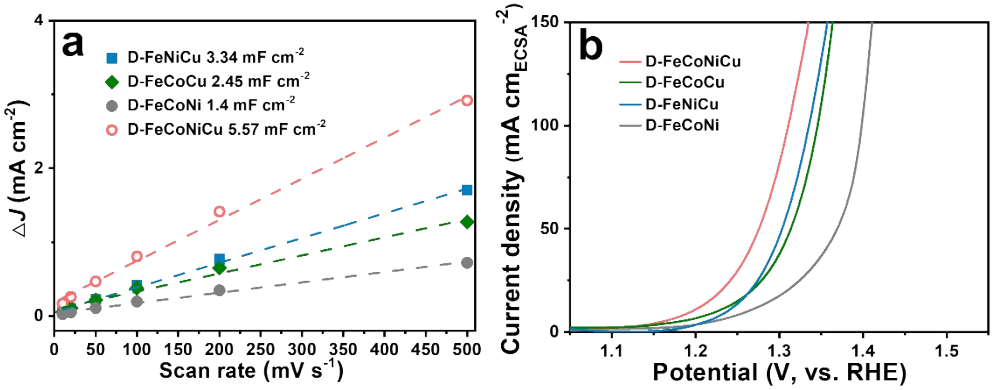

Figure S12. (a) The C_{dl} of D-FeCoNiCu-LDH/NF, D-FeNiCu-LDH/NF, D-FeCoCu-LDH/NF and D-FeCoNi-LDH/NF determined by the plots of $\Delta j/2$ against various scan rates at 0.32 V vs. RHE. The Δj is the difference between anodic and cathodic current densities in CVs at different scan rates at this potential. (b) ECSA-normalized LSV curves of D-FeCoNiCu-LDH/NF, D-FeNiCu-LDH/NF, D-FeCoCu-LDH/NF and D-FeCoNi-LDH/NF for GOR in 1.0 M KOH with 100 mM glucose.

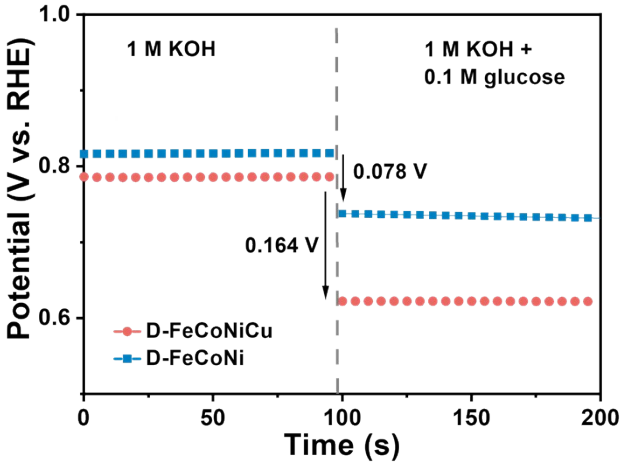

Figure S13. The OCP curves of D-FeCoNiCu-LDH/NF and D-FeCoNi-LDH/NF recorded in 1.0 M KOH without and with 100 mM glucose.

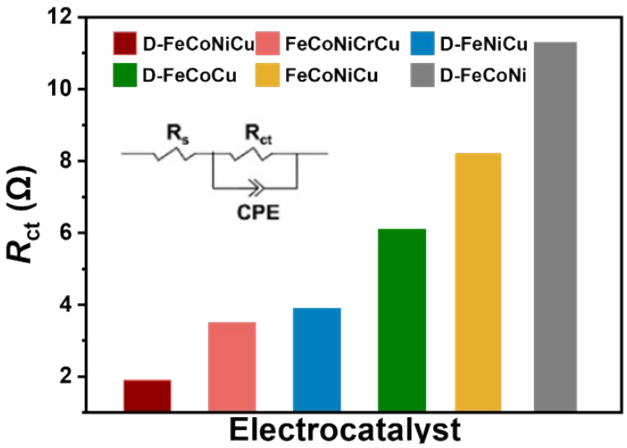

Figure S14. Equivalent circuit diagram and R_{ct} of electrocatalyst.

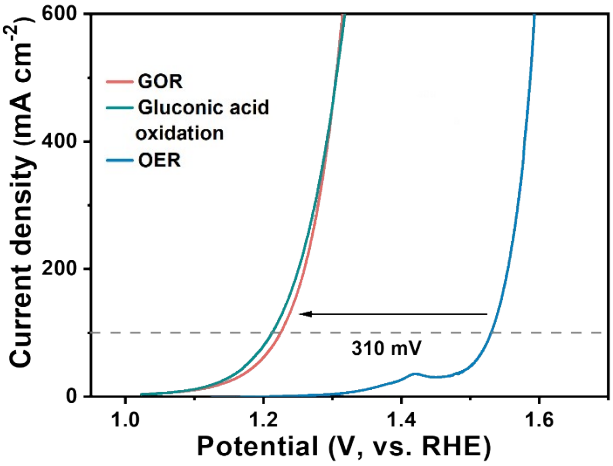

Figure S15. Comparison between GOR, gluconic acid oxidation and OER with D-FeCoNiCu-LDH/NF as electrocatalyst.

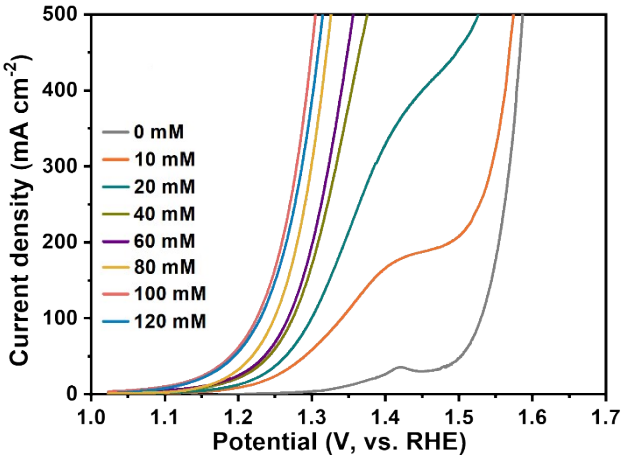

Figure S16. LSV profiles for oxidation of glucose with differing concentration and D-FeCoNiCu-LDH/NF as electrocatalyst.

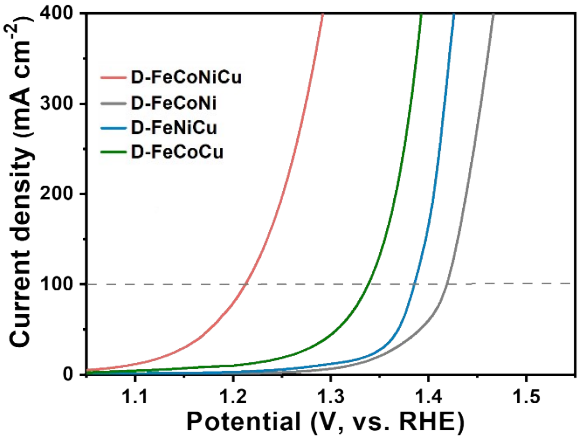

Figure S17. LSVs for D-FeCoNiCu-LDH/NF, D-FeNiCu-LDH/NF, D-FeCoCu-LDH/NF and D-FoCoNi-LDH/NF for gluconic acid electrooxidation in 1.0 M KOH with 0.1 M gluconic acid.

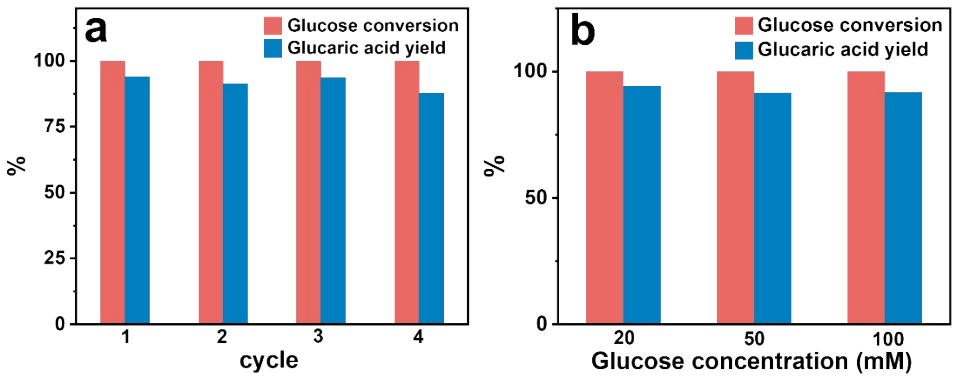

Figure S18. (a) Glucose conversion and glucaric acid yield using same D-FeCoNiCu-LDH/NF electrocatalyst in different cycle. (b) Glucose conversion and glucaric acid yield with differing concentration of substrate.

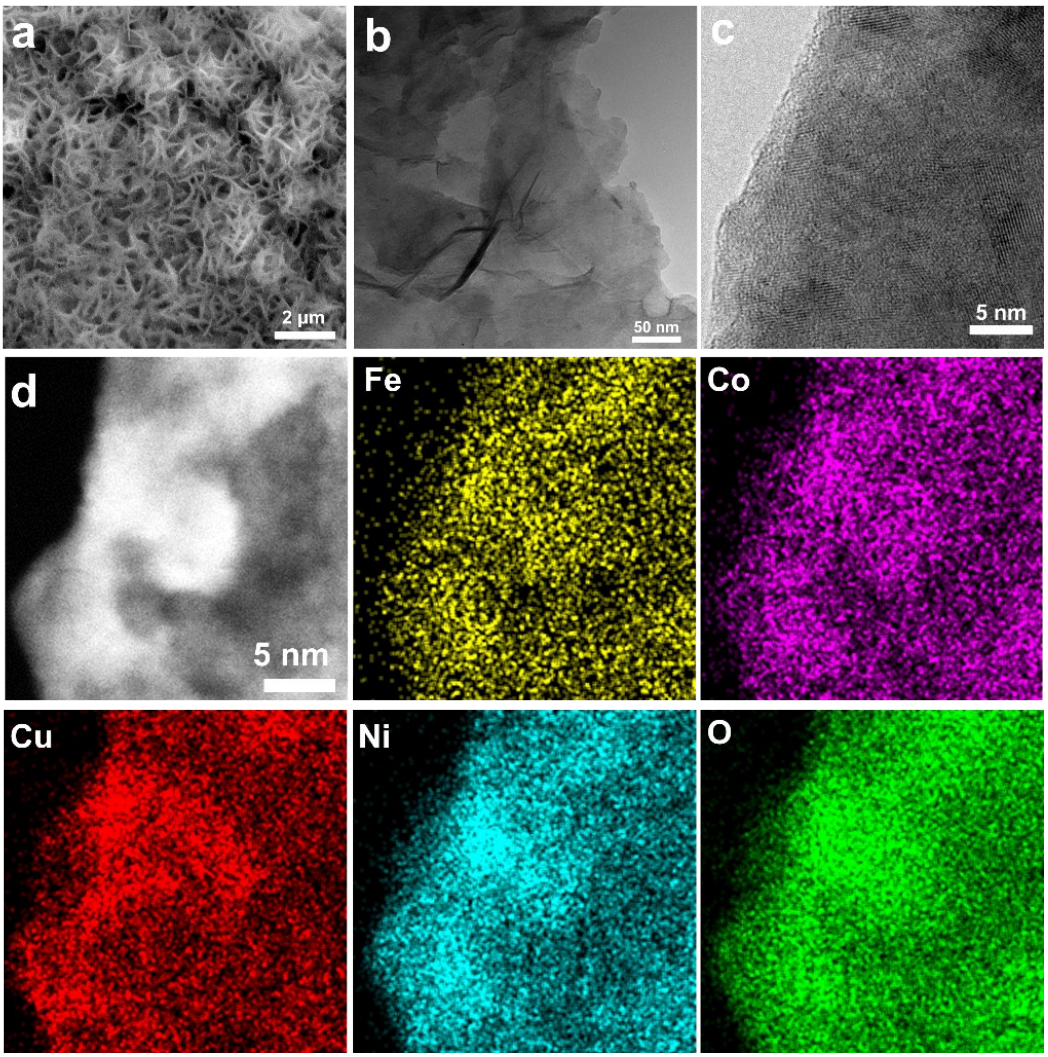

Figure S19. (a) SEM image of D-FeCoNiCu-LDH/NF following GOR. (b) TEM and (c) HRTEM, images of D-FeCoNiCu-LDH following GOR peeled from NF. (d) Elemental mapping evidencing presence and homogenous distribution of Fe, Co, Ni, Cu and O elements in D-FeCoNiCu-LDH following GOR.

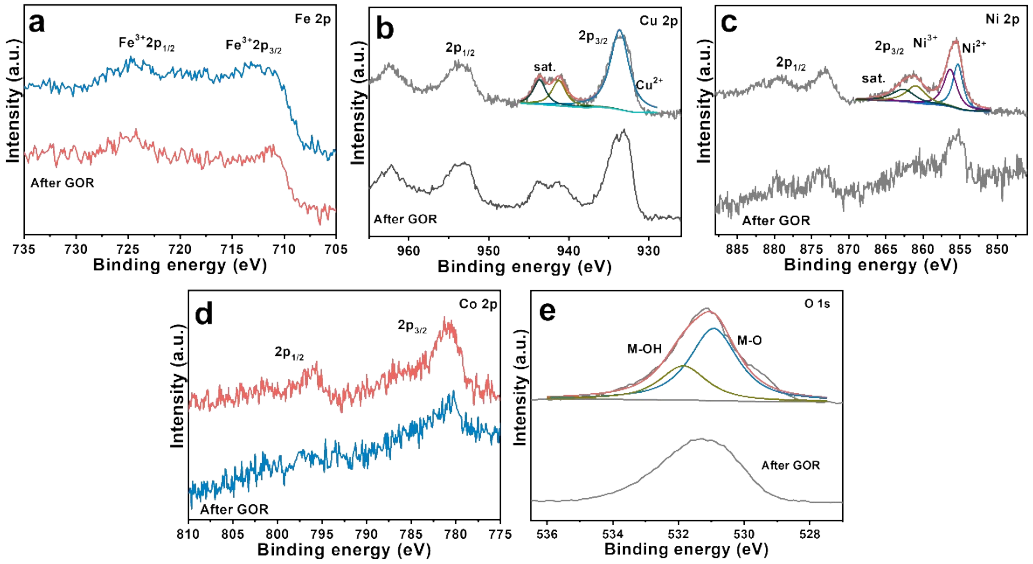

Figure S20. (a) Fe 2p, (b) Cu 2p, (c) Ni 2p, (d) Co 2p and (e) O 1s XPS spectra for D-FeCoNiCu-LDH/NF following GOR.

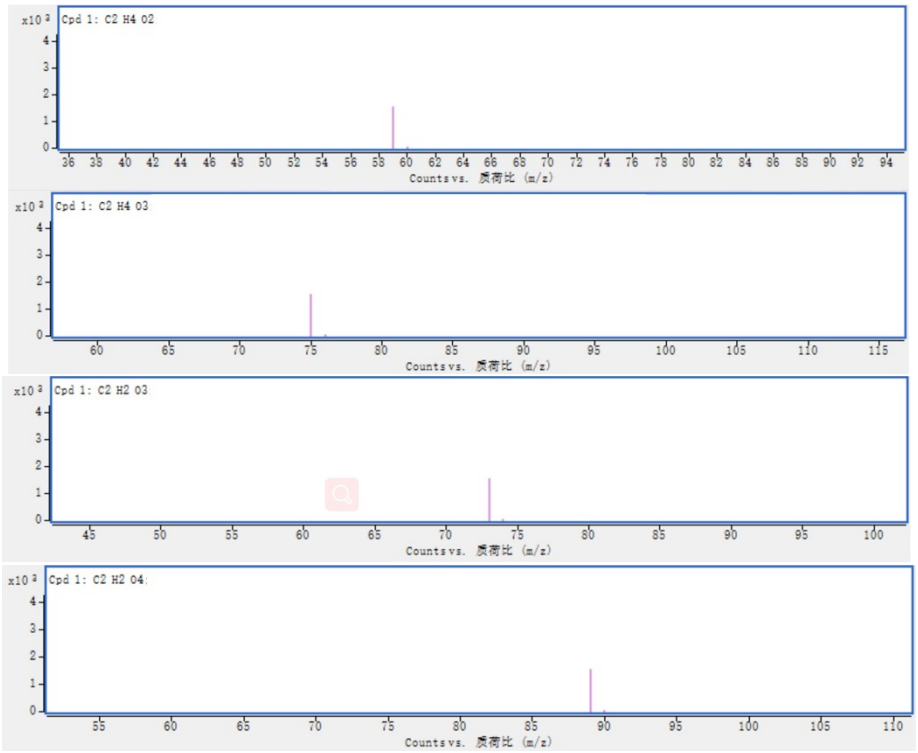

Figure S21. LC-MS findings for glycolaldehyde electrooxidation with D-FeCoNiCu-LDH/NF as electrocatalyst, showing the products are glycolic acid, glyoxylic acid and oxalic acid.

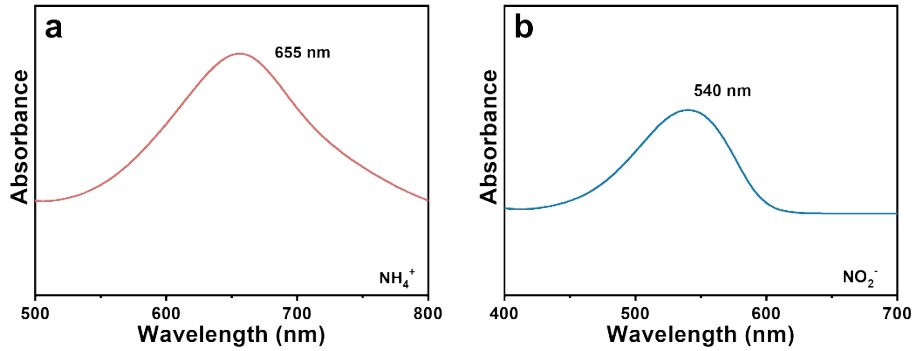

Figure S22. UV-Vis spectra confirming that products of NO_3^-RR are (a) NH_4^+ and (b) NO_2^-.

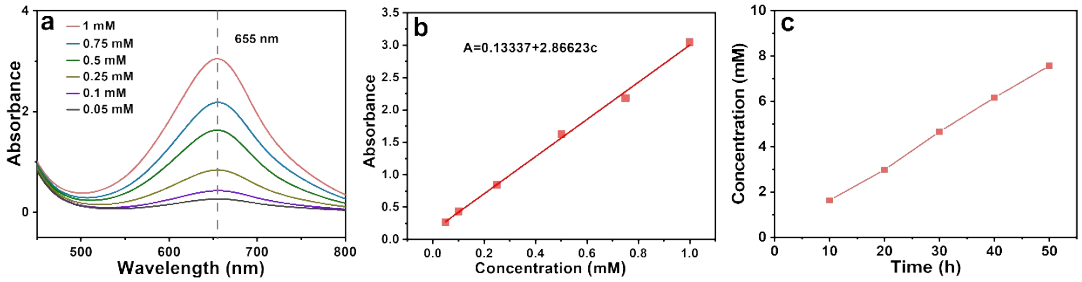

Figure S23. (a) UV-vis curves of different concentrations of NH_4^+. (b) Calibration curve of NH_4^+ concentration. (c) Concentration of NH_4^+ at different reaction times.

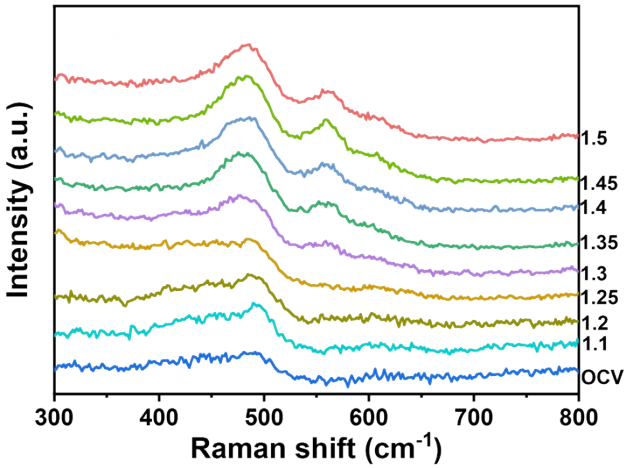

Figure S24. *In situ* Raman spectra for D-FeCoNiCu-LDH/NF electrode and corresponding structural conversion under changed potential in 1.0 M KOH with 0.1 M glucose solution.

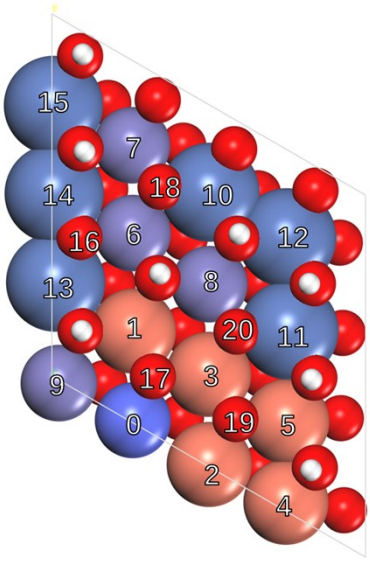

Figure S25. Schematic for initial site for placing adsorbent on globally searched stable D-FeNiCoCu-LDH structure.

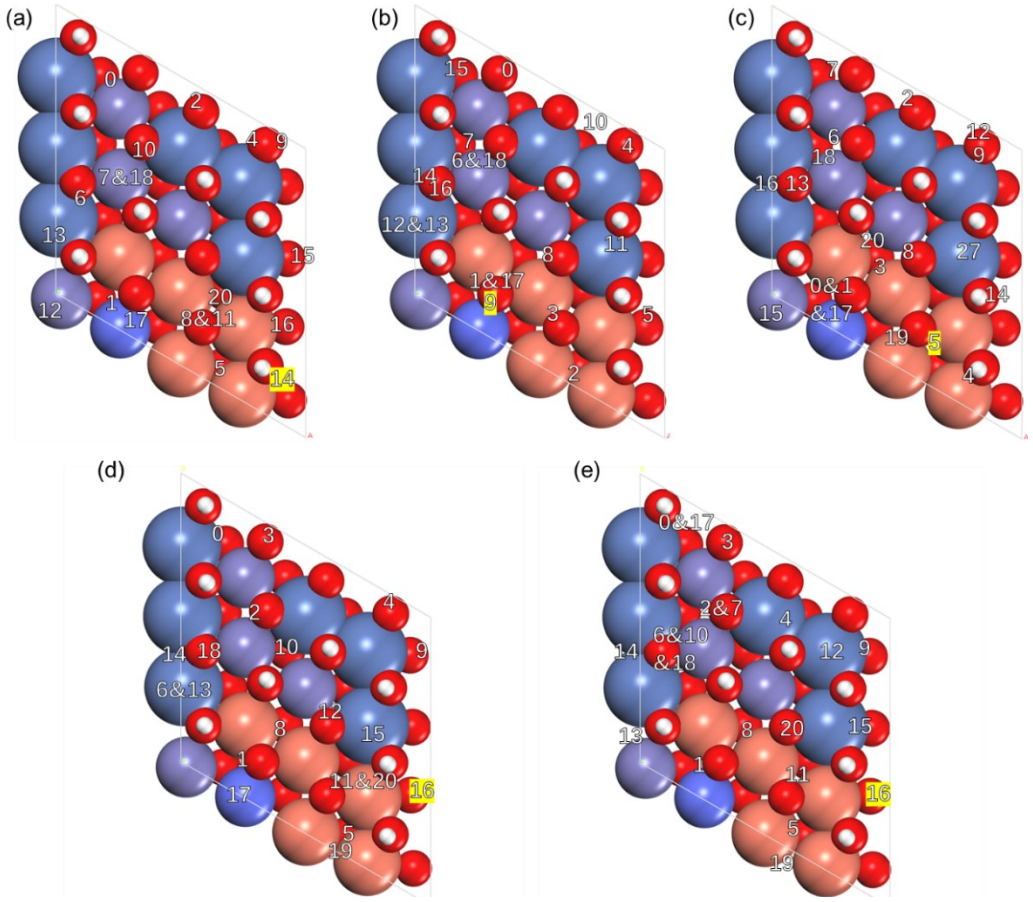

Figure S26. Schematic for adsorption site following relaxation for (a) glycolaldehyde, (b) glycolic acid, (c) *CO_2HCH_2O, (d) glyoxylic acid, and (e) oxalic acid. (Site with yellow-color is relative to most stable adsorption configurations).

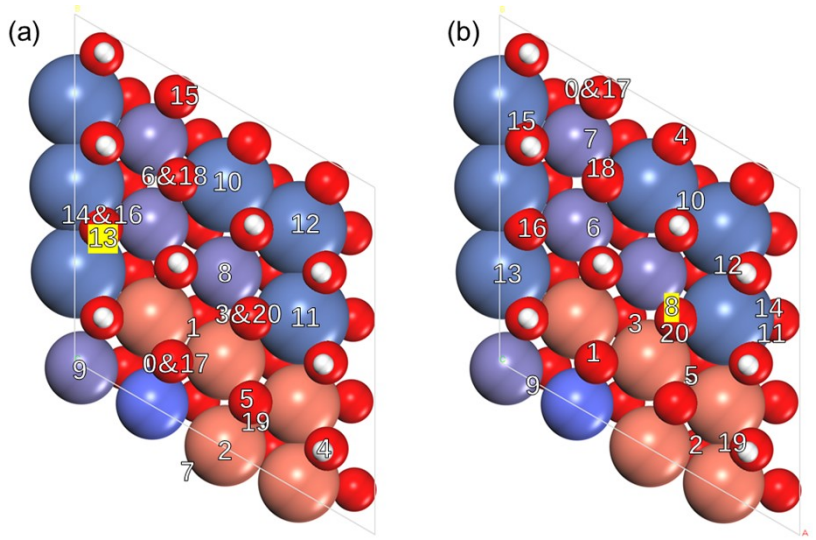

Figure S27. Schematic for adsorption site following relaxation for (a) glyoxal and (b) *CO_2HCHOH. (Site with yellow-color is relative to most stable adsorption configurations).

Table S1. Fitted parameters for Fe K-edge, Co K-edge, Ni K-edge and Cu K-edge EXAFS spectra.

Sample	Path	S_0^2 (amp)	C.N.	R [Å]	Rref [Å]	σ^2 [Å^2]	ΔE_0 [eV]
Co-foil	Co-Co	0.72	12 (fixed)	2.49 ± 0.01	2.50	0.0062 ± 0.0004	6.4 ± 0.4
FeCoNi CuCr-LDH	Co-O	0.72 (fixed)	6.0 ± 0.3	2.08 ± 0.01	2.13	0.0050 ± 0.0005	-1.5 ± 0.8
	Co-M		6.0 ± 0.5	3.13 ± 0.01	3.12	0.0089 ± 0.0008	
D-FeCoNi Cu-LDH	Co-O	0.72 (fixed)	6.1 ± 0.3	1.90 ± 0.01	1.93	0.0060 ± 0.0003	-6.3 ± 1.4
	Co-M		2.9 ± 1.2	2.84 ± 0.02	2.86	0.0081 ± 0.0004	
Fe-foil	Fe-Fe	0.72	8 (fixed)	2.46 ± 0.01	2.46	0.0049 ± 0.0007	4.8 ± 1.1
	Fe-Fe		6 (fixed)	2.85 ± 0.01	2.84	0.0049 ± 0.0007	
FeCoNi CuCr-LDH	Fe-O	0.72 (fixed)	6.2 ± 0.2	1.99 ± 0.01	1.94	0.0080 ± 0.0002	-3.8 ± 1.0
	Fe-M		3.6 ± 1.2	3.03 ± 0.01	2.97	0.0126 ± 0.0038	
D-FeCoNi Cu-LDH	Fe-O	0.72 (fixed)	6.0 ± 0.2	1.97 ± 0.01	1.94	0.0075 ± 0.0015	-4.2 ± 1.1
	Fe-M		3.4 ± 1.3	2.99 ± 0.02	2.97	0.0117 ± 0.0040	
Ni-foil	Ni-Ni	0.79	12 (fixed)	2.49 ± 0.01	2.44	0.0061 ± 0.0003	8.1 ± 0.4
FeCoNi CuCr-LDH	Ni-O	0.79 (fixed)	6.1 ± 0.5	2.07 ± 0.01	2.08	0.0065 ± 0.0014	-3.2 ± 0.7
	Ni-M		9.2 ± 1.5	3.13 ± 0.01	3.12	0.0145 ± 0.0020	
D-FeCoNi Cu-LDH	Ni-O	0.79 (fixed)	5.6 ± 0.7	2.02 ± 0.01	2.08	0.0069 ± 0.0019	-5.8 ± 1.1
	Ni-M		7.7 ± 2.6	3.06 ± 0.02	3.05	0.0184 ± 0.0044	
Cu-foil	Cu-Cu	0.95	12 (fixed)	2.54 ± 0.01	2.56	0.0088 ± 0.0006	4.8 ± 0.7
FeCoNi CuCr-LDH	Cu-O	0.95 (fixed)	3.0 ± 0.7	1.93 ± 0.02	1.94	0.0078 ± 0.0036	-6.9 ± 2.2
	Cu-M		6.6 ± 1.5	3.12 ± 0.03	3.15	0.0186 ± 0.0035	
D-FeCoNi Cu-LDH	Cu-O	0.95 (fixed)	3.4 ± 0.2	1.94 ± 0.01	1.94	0.0056 ± 0.0010	-2.4 ± 0.9
	Cu-M		2.5 ± 1.1	3.00 ± 0.03	2.95	0.0225 ± 0.0040	

C.N. = coordination number; S_0^2 = amplitude reduction factor; R = interatomic distance; Σ^2 = Debye-Waller factor; ΔE_0 = energy shift refers to the E_0 position.

Table S2. Comparison of D-FeCoNiCu-LDH/NF electrocatalyst with reported electrocatalysts for glucose oxidation.

Electrocatalyst	**Product(s)**	**Electrolyte**	**Voltage (V)**	**Current density (mA cm^{-2})**	**Ref.**
D-FeCoNiCu-LDH/NF	Glucaric acid	1.0 M KOH + 0.1 M glucose	1.22 1.26 1.30	100 200 500	This work
$NiFeO_x$-NF	Glucaric acid	1.0 M KOH + 0.1 M glucose	1.31	87.6	[10]
Fe_2P films	Gluconolactone	1.0 M KOH + 0.5 M glucose	1.39	100	[11]
CoOOH	Formate	1.0 M KOH + 0.1 M glucose	1.51	100	[12]
$Cu(OH)_2$	Gluconic acid	1.0 M KOH + 0.1 M glucose	1.49	100	[13]
PtO_x	gluconate	0.2 M PBS (pH = 7) + 0.1 M glucose	1.2	0.07	[14]

Table S3. Comparison of hybrid electrolytic cell for organics electrooxidation coupled with NO_3^-RR, or HER.

Electrocatalyst	Anode|| Cathode	Voltage (V)	Current density (mA cm^{-2})	Stability (h)	Ref.
D-FeCoNiCu-LDH/NF||FeCoNiCuCr-LDH/NF	GOR||NO_3^-RR	1.07 1.32 1.44	10 100 300	50	This work
	GOR||HER	1.17 1.43 1.54	10 100 200		
$NiFeO_x$-NF||$NiFeN_x$-NF	GOR||HER	1.39 1.48	100 200	24	[10]
Fe_2P/SSM||Pt/C	GOR||HER	1.22 1.58	10 100	24	[11]
Reconstructed-NiCu-OH||Reconstructed-NiCuO	Glycerol oxidation||NO_3^-RR	1.38 1.8	100 300	-	[15]
Ni foam||CoP nanosheet arrays/carbon fiber cloth	Benzyl alcohol oxidation||NO_3^-RR	1.49 1.6	10 50	6	[16]

Table S4. Adsorption energy for possible configurations for glycolaldehyde (*$C_2H_4O_2$) on D-FeNiCoCu-LDH.

No.	Adsorption site after relaxation	Adsorption Energy (eV)
14	**Cu-Ni Bridge**	-1.64
8 & 11	**Cu-Cu-Cu-O Top**	-1.61
9	**Cu-Fe-Ni-O Top**	-1.46
16	**Cu-Ni-Ni Hollow**	-1.43
20	**Cu-Cu-Ni Hollow**	-1.39
12	Fe-Ni Bridge	-1.25
5	**Cu-Cu-Cu Hollow**	-1.21
6	Ni-Ni-Fe-O Top	-1.16
4	**Cu-Ni Bridge**	-1.12
13	Ni Top	-1.12
17	Co Top	-1.06
2	**Cu-Cu-Ni-O Top**	-0.98
10	Fe-Fe-Ni Hollow	-0.91
7 & 18	Fe Top	-0.88
0	Fe-Co Bridge	-0.83
1	**Cu-Co Bridge**	-0.72
15	Ni-Ni-Ni Hollow	-0.48

Table S5. Adsorption energy for possible configurations for glycolic acid (*$C_2H_4O_3$) on D-FeNiCoCu-LDH. (Adsorption energy is relative to most stable glycolaldehyde-adsorbed configurations).

No.	Adsorption site after relaxation	Relative Adsorption Energy (eV)
9	**Cu-Co Bridge**	-0.43
6 & 18	Fe-Fe Bridge	-0.34
4	**Cu-Fe-Ni-O Top**	-0.32
12 & 13	Ni Top	-0.27
11	Ni Top	-0.18
5	**Cu-Ni-Ni Hollow**	-0.14
7	Fe-Fe Bridge	-0.05
10	**Cu-Ni-Ni Hollow**	0.05
3	**Cu-Cu-Cu-O Top**	0.07
1 & 17	**Cu-Cu-Co-O Top**	0.10
8	**Cu-Fe-Ni-O Top**	0.14
14	Ni-Ni-Fe-O Top	0.32
15	Fe-Ni-Co Hollow	0.37
2	**Cu-Cu Bridge**	0.40
16	Ni-Ni-Fe-O Top	0.44
0	**Cu-Cu-Co-O Top**	0.45

Table S6. Adsorption energy for possible configurations for $*CO_2HCH_2O$ on D-FeNiCoCu-LDH. (Adsorption energy is relative to most stable glycolaldehyde-adsorbed configurations).

No.	Adsorption site after relaxation	Relative Adsorption Energy (eV)
5	**Cu-Cu Bridge**	0.19
6	Fe-Fe Bridge	0.21
18	Fe-Fe Bridge	0.31
20	**Cu-Fe Bridge**	0.32
0 & 1 & 17	**Cu-Co Bridge**	0.36
2	**Ni-Cu Bridge**	0.39
16	Ni-Ni Bridge	0.43
7	Co-Fe Bridge	0.50
19	**Cu-Cu Bridge**	0.53
11	Ni Top	0.56
3	**Cu-Cu-Fe Hollow**	0.60
8	**Cu-Fe Bridge**	0.63
9	Fe-Ni Bridge	0.84
12	**Cu-Ni-Ni-O Top**	1.71
13	Fe-Ni-Ni-O Top	1.82
15	Fe-Ni Bridge	1.94
4	**Cu-Cu Bridge**	2.01
14	**Cu-Ni-Ni-O Top**	2.61

Table S7. Adsorption energy for possible configurations for glyoxylic acid (*$C_2H_2O_3$) on D-FeNiCoCu-LDH. (Adsorption energy is relative to most stable glycolaldehyde-adsorbed configurations).

No.	Adsorption site after relaxation	Relative Adsorption Energy (eV)
16	**Cu-Ni Bridge**	0.61
6 & 13	Ni Top	0.65
4	**Cu-Ni-Fe Hollow**	0.90
9	Ni-Ni-Fe Hollow	1.00
18	Fe-Ni-Ni-O Top	1.12
0	Fe-Co-Ni-O Top	1.25
11 & 20	**Cu-Cu Bridge**	1.27
2	Fe-Fe-Ni-O Top	1.28
17	Co Top	1.49
1	**Cu-Co Bridge**	1.54
19	**Cu-Cu Bridge**	1.56
3	**Fe-Co-Cu-O Top**	1.66
14	Ni-Ni Bridge	1.69
10	Fe-Ni-Fe Hollow	1.73
5	**Cu-Cu-Cu Hollow**	1.74
12	**Fe-Cu-Ni-O Top**	1.78
8	**Cu-Cu Bridge**	2.02
15	Ni Top	2.24

Table S8. Adsorption energy for possible configuration for oxalic acid ($*C_2H_2O_4$) on D-FeNiCoCu-LDH. (Adsorption energy is relative to most stable glycolaldehyde-adsorbed configurations).

No.	Adsorption site after relaxation	Relative Adsorption Energy (eV)
16	**Cu-Ni Bridge**	0.38
13	**Cu-Ni-Fe Hollow**	0.62
6 & 10 & 18	Fe-Fe-Ni-O Top	0.82
9	Ni-Ni Bridge	0.89
12	Ni Top	0.97
20	**Cu-Fe-Ni-O Top**	1.09
11	**Cu-Cu Bridge**	1.16
14	Ni-Ni Bridge	1.16
0 & 17	Co-Ni-Fe Hollow	1.20
2 & 7	Fe-Fe-Ni-O Top	1.28
5	**Cu-Cu-Cu Hollow**	1.31
1	**Cu-Co Bridge**	1.39
3	**Cu-Co-Cu-O Top**	1.40
4	Ni-Ni Bridge	1.56
19	**Cu-Ni Bridge**	1.64
8	**Cu-Cu-Fe Hollow**	1.92
15	Ni Top	2.10

Table S9. Adsorption energy for possible configurations for glyoxal (*$C_2H_2O_2$) on D-FeNiCoCu-LDH. (Adsorption energy is relative to most stable glycolaldehyde-adsorbed configurations).

No.	Adsorption site after relaxation	Relative Adsorption energy (eV)
13	Fe-Ni-Ni-O top site	1.12
14 & 16	Fe-Ni-Ni-O top site	1.49
3 & 20	**Cu-Fe-Ni-O top site**	1.53
6 & 18	Fe-Fe-Ni-O top site	1.55
15	**Fe-Co-Cu-O top site**	1.55
5	**Cu-Cu-Cu-O top site**	1.56
19	**Cu-Cu-Cu-O top site**	1.68
0 & 17	**Cu-Cu-Co-O top site**	1.72
2	**Cu top site**	1.81
7	**Cu-Fe bridge site**	2.06
1	**Cu-Cu bridge site**	2.10
4	**Cu-Cu-Ni-O top site**	2.20
11	Ni top site	2.22
9	Fe top site	2.24
10	Ni top site	2.26
12	Ni top site	2.29
8	Fe top site	2.51

Table S10. Adsorption energy for possible configurations for *CO_2HCHOH on D-FeNiCoCu-LDH. (Adsorption energy is relative to most stable glycolaldehyde-adsorbed configurations).

No.	Adsorption site after relaxation	Relative Adsorption energy (eV)
8	**Cu-Fe-Ni-O Top**	-0.39
1	**Cu-Cu-Co-O Top**	-0.18
18	Fe-Fe-Ni-O Top	-0.17
4	**Cu-Cu-Ni-O Top**	-0.07
5	**Cu-Cu Bridge**	-0.03
16	Fe-Ni-Ni-O Top	-0.02
20	**Cu-Fe-Ni-O Top**	0.06
6	Fe Top	0.11
0 & 17	**Cu-Fe-Co-O Top**	0.30
2	**Cu-Cu-Cu Hollow**	0.31
3	**Cu-Cu-Fe Hollow**	0.35
15	Fe-Ni Bridge	0.46
11	Ni-Ni Bridge	0.50
7	Fe Top	0.51
19	**Cu-Cu Bridge**	0.52
14	Ni-Ni Bridge	0.53
12	Ni-Ni Bridge	0.59
13	Ni Top	0.61
10	Ni-Ni Bridge	0.61
9	Fe-Co Bridge	0.91

References

1. B. Ravel and M. Newville, *J. Synchrotron Rad.*, 2005, **12**, 537-541.
2. R. Singh, A. Sharma, P. Singh, G. Balasubramanian and D. D. Johnson, *Nat. Comput. Sci.*, 2021, **1**, 54-61.
3. J. M. Rickman, H. M. Chan, M. P. Harmer, J. A. Smeltzer, C. J. Marvel, A. Roy and G. Balasubramanian, *Nat. Commun.*, 2019, **10**.
4. M. Van den Bossche, H. Grönbeck and B. Hammer, *J Chem. Theory Comput.*, 2018, **14**, 2797-2807.
5. V. L. Deringer, A. P. Bartók, N. Bernstein, D. M. Wilkins, M. Ceriotti and G. Csányi, *Chem. Rev.*, 2021, **121**, 10073-10141.
6. J. Zhang and V. A. Glezakou, *Int. J. Quantum Chem.*, 2020, **121**, e26553.
7. J. P. Perdew, W. Yang, K. Burke, Z. Yang, E. K. U. Gross, M. Scheffler, G. E. Scuseria, T. M. Henderson, I. Y. Zhang, A. Ruzsinszky, H. Peng, J. Sun, E. Trushin and A. Görling, *PNAS*, 2017, **114**, 2801-2806.
8. J. P. Perdew, K. Burke and M. Ernzerhof, *Phys. Rev. Lett.*, 1996, **77**, 3865-3868.
9. P. E. Blöchl, *Phys. Rev. B*, 1994, **50**, 17953-17979.
10. W. J. Liu, Z. Xu, D. Zhao, X. Q. Pan, H. C. Li, X. Hu, Z. Y. Fan, W. K. Wang, G. H. Zhao, S. Jin, G. W. Huber and H. Q. Yu, *Nat. Commun.*, 2020, **11**, 265.
11. P. Du, J. Zhang, Y. Liu and M. Huang, *Electrochem. Commun.*, 2017, **83**, 11-15.
12. Y. Q. Zhu, H. Zhou, J. Dong, S. M. Xu, M. Xu, L. Zheng, Q. Xu, L. Ma, Z. Li, M. Shao and H. Duan, *Angew. Chem. Int. Ed.*, 2023, **62**, e202219048.
13. Y. Zhang, B. Zhou, Z. Wei, W. Zhou, D. Wang, J. Tian, T. Wang, S. Zhao, J. Liu, L. Tao and S. Wang, *Adv. Mater.*, 2021, **33**, 2104791.
14. E. v. K. Matthijs P. J. M. van der Ham, Marc T. M. Koper, Akbar Asadi Tashvigh, and Johannes H. Bitter, *Angew. Chem. Int. Ed.*, 2023, 62, e202306701.
15. S. Li, P. Ma, C. Gao, L. Liu, X. Wang, M. Shakouri, R. Chernikov, K. Wang, D. Liu, R. Ma and J. Wang, *Energy Environ. Sci.*, 2022, **15**, 3004-3014.
16. S. Ye, Z. Chen, G. Zhang, W. Chen, C. Peng, X. Yang, L. Zheng, Y. Li, X. Ren, H. Cao, D. Xue, J. Qiu, Q. Zhang and J. Liu, *Energy Environ. Sci.,*, 2022, **15**, 760-770.